PAPER

Check for updates

In situ synthesis of nanostructured Fe₃O₄@TiO₂ composite grown on activated carbon cloth as a binder-free electrode for high performance supercapacitors†

Hai Wang, [iD] *[ab] Xingping Xu[a] and Anne Neville[b]

Transition metal oxide (TMO) nanomaterials with regular morphology have received widening research attention as electrode materials due to their improved electrochemical characteristics. In this study we present the successful fabrication of an Fe₃O₄/TiO₂ nanocomposite grown on a carbon cloth (Fe₃O₄/TiO₂@C) used as a high-efficiency electrochemical supercapacitor electrode. Flexible electrodes are directly used for asymmetric supercapacitors without any binder. The increased specific surface area of the TiO₂ nanorod arrays provides sufficient adsorption sites for Fe₃O₄ nanoparticles. An asymmetric supercapacitor composed of Fe₃O₄/TiO₂@C is tested in 1 M Na₂SO₃ electrolyte, and the synergistic effects of fast reversible Faraday reaction on the Fe₃O₄/TiO₂ surface and the highly conductive network formed by TiO₂@C help the electrode to achieve a high areal capacitance of 304.1 mF cm⁻² at a current density of 1 mA cm⁻² and excellent cycling stability with 90.7% capacitance retention at 5 mA cm⁻² after 10 000 cycles. As a result, novel synthesis of a binder-free Fe₃O₄/TiO₂@C electrode provides a feasible approach for developing competitive candidates in supercapacitor applications.

1. Introduction

Energy storage devices which provide a clean and efficient energy source have been extensively explored in recent years to meet the needs of sustainable development. Converting renewable energy (such as wind energy, solar energy, *etc.*) into electrical energy is an efficient and convenient energy storage strategy.[1] Electrochemical capacitors, also known as supercapacitors (SCs), are energy storage devices integrated in rechargeable batteries and conventional capacitors.[2,3] SCs have drawn significant attention for their advantages of higher power density, faster charge/discharge and good cycling stability and can be widely used in electric vehicles, renewable energy power generation systems, aerospace and other fields.[4–6] SCs have become one of the most important energy conversion and storage systems in renewable and sustainable nanotechnology

in recent years. Electric double-layer capacitors (EDLCs) represented by carbon-based materials (MWCNT, rGO, AC, *etc.*) physically store charges *via* reversible ion adsorption on electrode/electrolyte interfaces for energy storage.[7–10] Enhanced specific surface area, low cost and compatibility with various electrolytes make EDLCs suitable candidates for commercial supercapacitors. In order to achieve higher capacitance than EDLCs, electrochemically active materials are also developed for supercapacitors applications, which are categorized as pseudocapacitors (PCs).[11,12] Different from the non-Faraday process on the EDLC surface, PCs relay on reversible faradic oxidation–reduction reactions at active sites to accumulate pseudo-capacitance for energy storage. Due to the existence of multiple redox states, transitions such as NiOₓ, RuO₂, MnO₂ and TiO₂ have shown immeasurable potential in the exploitation of electrode materials for PCs owing to high specific capacitance, low internal resistance and flexibility in shape management.[13–16] Among them, nanosized magnetite (Fe₃O₄) is one of the promising materials that has potential prospects in applications such as high-efficiency sodium-ion batteries (SIBs) and supercapacitors.[17,18] Apart from Fe₃O₄, titanium dioxide (TiO₂) has been recognized as a promising alternative for electronic applications due to its advantages of low cost, low toxicity, natural abundance and chemical stability.[19–21] Additional efforts towards increasing the exposed area and achieving better electrochemical performances have been made to take full advantages of TiO₂. To address this issue, one-dimensional

[a]College of Mechanical and Electronic Engineering, China University of Petroleum (East China), Qingdao, 266580, China

[b]Institute of Functional Surfaces, School of Mechanical Engineering, University of Leeds, Leeds, LS2 9JT, UK. E-mail: mnhw@leeds.ac.uk

† Electronic supplementary information (ESI) available: Ultraviolet absorption spectroscopy of Fe₃O₄/TiO₂@C product (Fig. S1), local EDX mapping of Fe₃O₄/TiO₂@C electrode of the certain area (Fig. S2), integrated CV area and corresponding capacitance of Fe₃O₄/TiO₂@C electrode at the cycle number of 1, 2500, 5000 and 10 000 respectively (Table S1), load mass of active material and specific capacitance measured by mass ratio (Table S2). See DOI: 10.1039/d1ra04424a

(1D) nanostructured TiO_2 with a larger surface area and more active sites could provide the electrode framework with an optimal ion diffusion path through the electrolyte and into the solid center, thereby reducing internal resistance and improving pseudo-capacitance performance.[22–24] Homogeneous and vertically arranged nanorods have many advantages in energy storage applications. Raj[25] reported the optimization of carrier density of the TiO_2 nanotube electrodes for supercapacitor applications with an ultra-high carrier density of 2.73×10^{22} cm^{-3}, and a remarkable area capacitance of 20.09 mF cm^{-2} was observed at the discharge rate of 0.1 mA cm^{-2}. Gu[26] deposited TiO_2 nanowires (TiO_2@CC) arrays on carbon cloth using a solution-based technique at 80 °C and in an open atmosphere. The high specific surface area and good pore structure give the TiO_2@CC electrode an areal capacitance of 1204.8 mF cm^{-2}. Moreover, the TiO_2@CC supercapacitor also shows good stability and flexibility. Wang[27] synthesized TiO_2–C@polyaniline (PANI) flexible electrode on the surface of carbon cloth (CC), in which TiO_2–C nanowire array (NWAS) was used as a supporting framework to enhance the mechanical stability and PANI coated TiO_2–C NWA helped form a core–shell structure. TiO_2–C@PANI has a remarkable capacitance of 1818 F g^{-1} at current density of 1 A g^{-1} and a capacity retention of 80% after 5000 cycles. Combining the superior advantages of TiO_2 nanorod arrays with other components in manufacturing Metal–Organic Framework (MOF) or Covalent Organic Framework (COF) proves to be an effective way to improve capacitance strategically. Although there have been research reports on the combination of Fe_3O_4 and TiO_2 nanorod arrays, few research has been focused on improving their electrochemical performance. On the other hand, particle agglomeration and limited ion diffusion movement are still the main reasons restricting the utilization of Fe_3O_4/TiO_2 materials in energy storage applications.

Herein, we report the *in situ* preparation of a 3D interconnected Fe_3O_4/TiO_2@C porous structure for supercapacitor electrodes on a carbon cloth substrate by hydrothermal and chemical deposition, in which TiO_2 nanorod arrays are grown vertically on a carbon cloth by hydrothermal method and then immersed in $FeCl_3$ solution and calcined in a mixture of Ar and H_2. Nano-sized Fe_3O_4 grows on the dendrite of TiO_2 microflowers and forms a conductive network between TiO_2–C nanowires. TiO_2 nanorods with a diameter of 100 nm are assembled into porous micro-flowers which induces TiO_2 nanorods to vertically grow on substrate. Investigations on the morphology, microstructure and electrochemical properties show that Fe_3O_4/TiO_2@C is an integrated electrode with high energy density and cyclic stability. This simple and effective synthesis of Fe_3O_4/TiO_2@C electrodes offers new opportunities for rational design and manufacture of high-performance TiO_2-based materials for energy storage devices.

2. Materials and methods

2.1 Material preparation

Iron(III) chloride hexahydrate ($FeCl_3 \cdot 6H_2O$) was purchased from VWR Chemicals (USA). Titanium butoxide ($C_{16}H_{36}O_4Ti$),

hydrochloric acid (HCl) were purchased from Sigma-Aldrich, carbon cloth was purchased from HeShi New Materials Co., Ltd. All the chemicals were used as received without further purification.

2.2 *In situ* synthesis of Fe_3O_4/TiO_2@C composites

TiO_2 nanorod arrays were first grown on the carbon cloth by a hydrothermal method as follows. The carbon cloth substrate was first cleaned with acetone and deionized water for 5 min respectively then placed in reaction solution. The reaction solution consisted of HCl (20 mL), H_2O (20 mL) and different amount of titanium butoxide (0.5 mL, 1 mL, 2.5 mL and 5 mL). Afterwards, the solution was poured into a Teflon-liner stainless steel autoclave with the carbon cloth substrate and kept at 250 °C for 6 h. Afterward, the sample was rinsed and annealed at 450 °C for 1 h in Ar atmosphere. Then, the Fe_3O_4 was anchored on the above TiO_2 nanorod arrays by a chemical deposition method. The TiO_2 nanorod arrays were immersed into $FeCl_3$ solution (0.1 mol L^{-1}) for 3 h and then rinsed and dried. Finally, the sample was annealed at 400 °C in Ar (95%) + H_2 (5%) for 1 h to obtain TiO_2/Fe_3O_4 composite arrays. The samples were named as Fe_3O_4/TiO_2@C-1, Fe_3O_4/TiO_2@C-2, Fe_3O_4/TiO_2@C-3 and Fe_3O_4/TiO_2@C-4 respectively according to the increasing amount of titanium butoxide added in the reaction solution.

2.3 Material characterisation

The morphology of the products was observed by scanning electron microscopy (SEM, JSM7610plus), the crystal structure of the composites was obtained using X-ray photoelectron spectroscopy (XPS, Thermal Scientific ESCALAB Xi$^+$) and X-ray diffraction (Rigaku XRD ULTIMA IV). The structure and elemental composition of the products was characterized by ultraviolet absorption spectrum (UV, PerkinElmer Lambda 35) and electron energy-dispersive X-ray spectroscopy (EDX, Thermo Scientific UltraDry EDS).

2.4 Fabrication of a supercapacitor electrode

The product Fe_3O_4/TiO_2@C can be directly used as electrode without any binder or post-processing for supercapacitors. In order to calculate the areal capacitance, the electrode was cut into a square chip (area = 1 cm × 1 cm). Consequently, the area of Fe_3O_4/TiO_2@C electrode was calculated as 1 cm^{-2} for determining areal capacitance. The loading mass of the active material is measured by the weight difference before and after *in situ* synthesis to calculate specific capacitance.

2.5 Electrochemical characterization of Fe_3O_4/TiO_2@C supercapacitor

Electrochemistry tests were conducted in a standard three-electrode system. The electrolyte is 1 mol L^{-1} Na_2SO_3 solution with the platinum foil as the counter electrode and a saturated silver/silver chloride as the reference electrode. The galvanostatic charge/discharge tests (GCD) at various current densities, cyclic voltammetry (CV) and
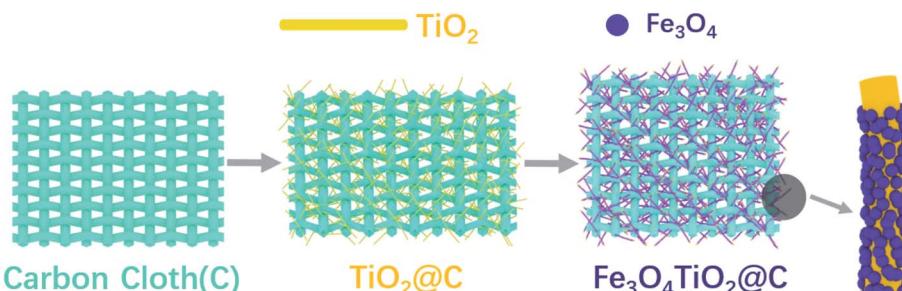
Fig. 1 Schematic diagram of fabrication process of Fe_3O_4/TiO_2@C electrode.

electrochemical impedance spectroscopy (EIS) tests were performed at room temperature using an CS150H electro-chemical workstation (Wuhan Corrtest Electronics Instruments Co., Ltd.). For the Fe_3O_4/TiO_2@C electrode, CV measurement was performed at a potential range of −1.1 V and 0.15 V *versus* silver/silver chloride. The AC impedance test frequency ranged from 100 kHz to 10 mHz.

The specific capacitance is calculated from GCD according to the following equation:[28]

$$C_s = I\frac{\Delta t}{s\Delta V} \qquad (1)$$

where C_s (mF cm^{-2}) is the areal capacitance, I (A) represent the discharge current, s (cm^{-2}), ΔV (V) and Δt (s) represent the area of the electrode, the potential drop during discharge and the total discharge time, respectively.

The specific capacitance calculated from CV curve is illustrated as the following equation:[29]

$$C_a = \frac{\int_{V_1}^{V_2} I(V)\nu dV}{s(V_2 - V_1)\nu} \qquad (2)$$

where C_a is the areal capacitance (mF cm^{-2}) according to CV, the integral represents the area under CV curve, s (cm^{-2}) is the area of the electrode, V_2 is the charge potential (V) and V_1

(V) is the discharge potential and ν is the scanning rate (mV s^{-1}).

3. Results and discussion

3.1 Microstructure and morphology characterizations

As is shown in Fig. 1, the Fe_3O_4/TiO_2@C electrode was fabricated by a simple two-step process. The displacement TiO_2 nanowire arrays were grown vertically on the surface of the carbon cloth through a hydrothermal process, and then calcined in Ar atmosphere at 450 °C to obtain TiO_2–C. Afterwards, magnetic Fe_3O_4 nanoparticles were fixed on vertically grown TiO_2 nanorod arrays *via* chemical deposition method and the product was annealed at 400 °C in Ar (95%) + H$_2$ (5%) to obtain the final product Fe_3O_4/TiO_2@C. The carbon cloth with staggered structure is used both as substrate and collector, which simplifies the fabrication process and enhances flexibility.

The crystal structure, morphology and microstructure of Fe_3O_4/TiO_2@C composites were studied by XRD, SEM, XPS and UV spectra. The SEM images of Fe_3O_4/TiO_2@C-3 composites are provided in Fig. 2(a)–(e). It can be clearly seen that the titanium dioxide nanorod array with high density and orderly arrangement were formed on the carbon cloth substrate. The TiO_2 nanorods are uniform in length, with an average diameter of
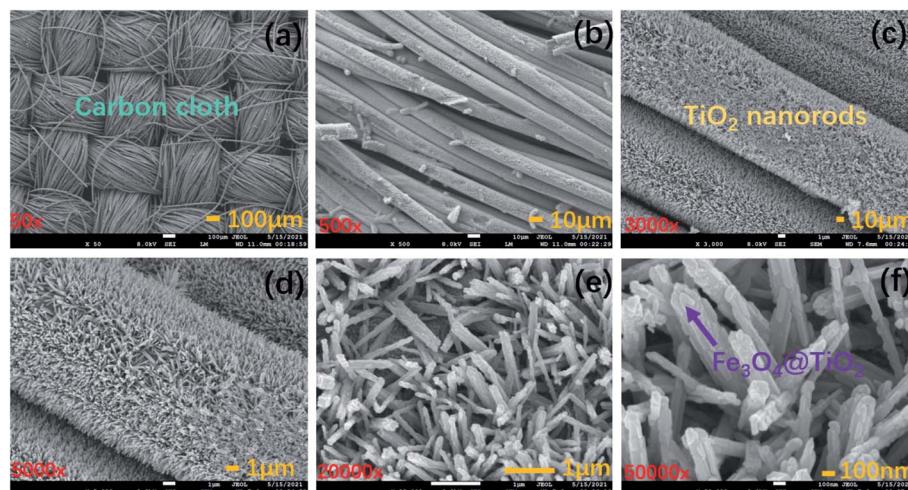

Fig. 2 (a)–(d) Low magnification SEM images of Fe_3O_4/TiO_2@C-3, and (e) and (f) high magnification SEM images of Fe_3O_4/TiO_2@C-3 composite.
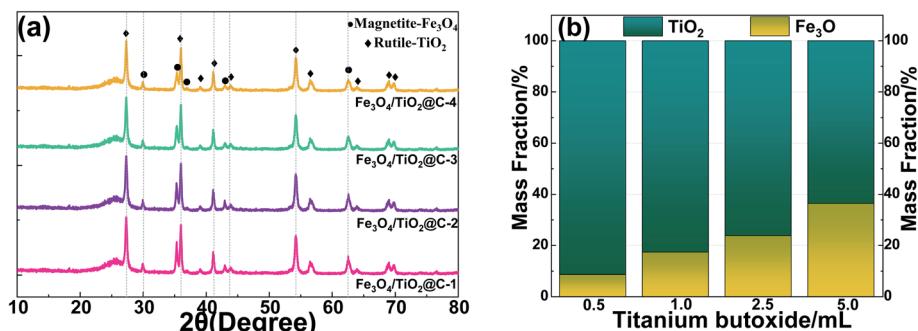
Fig. 3 (a) XRD patterns of $Fe_3O_4/TiO_2@C$ composites, (b) mass fraction of Fe_3O_4/TiO_2 with various titanium butoxide precursor.

about 100 nm and a rectangular cross-section. Fe_3O_4 is attached to the titanium dioxide nanorods and they are composed of smaller nanocrystals. As the framework of Fe_3O_4, TiO_2 nanorods interconnect with Fe_3O_4 to form a network structure.[30] TiO_2 nanorods array provides a larger exposed area, promoting electrolyte penetration and reducing resistance in charge transport, which is benefit for ion diffusion and storage on the electrode surface. Besides, the carbon cloth substrate provides a charge transfer channel with high conductivity for TiO_2/Fe_3O_4. The adhesion between TiO_2/Fe_3O_4 and the carbon cloth substrate can be produced by van der Waals interaction.[31,32] UV-vis absorption spectra in Fig. S1 in the ESI† showed a strong absorption band from 250 nm to 310 nm, which was related to the band edge absorption of TiO_2.

The XRD pattern of the prepared $Fe_3O_4/TiO_2@C$ composites with different amount of precursor solution is shown in Fig. 3(a). Characteristic peaks at $2\theta = 27.4$, 35.9, 41.31, 54.4,

56.7, 64.0 and 69.1° can be well indexed to (1 1 0), (1 0 1), (1 1 1), (2 1 1), (2 2 0) (3 0 1) and (3 0 1) crystal surface of TiO_2 respectively, which agrees well with the standard rutile phase of TiO_2 (JCPDS 21-1276). Peaks at $2\theta = 30.1°$, 35.5°, 43.1°, 56.9°, 62.5° and 74.5 are assigned to (2 2 0), (3 1 1), (4 0 0), (5 1 1), (4 4 0) and (5 3 3) planes of a typical magnetite phase Fe_3O_4 (JCPDS no. 19-0629).[33,34] No additional impurity peaks were detected, indicating the high purity of Fe_3O_4/TiO_2 and highly crystallized degree. The broad peak near 25 degrees is caused by the incomplete annealing of few TiO_2 at the calcination temperature of 400 °C.[35] As larger amount of titanium butoxide is added during hydrothermal process, the peak intensity of rutile phase increases compared with magnetite, indicating a higher mass fraction of TiO_2 content in the $Fe_3O_4/TiO_2@C$ composite. Specific amount of Fe_3O_4 and TiO_2 were calculated by XRD fitting peak quantitative analysis in Fig. 3(b). The mass fraction of Fe_3O_4 were 8.6%, 17.2%, 23.6% and 36.3% for $Fe_3O_4/$
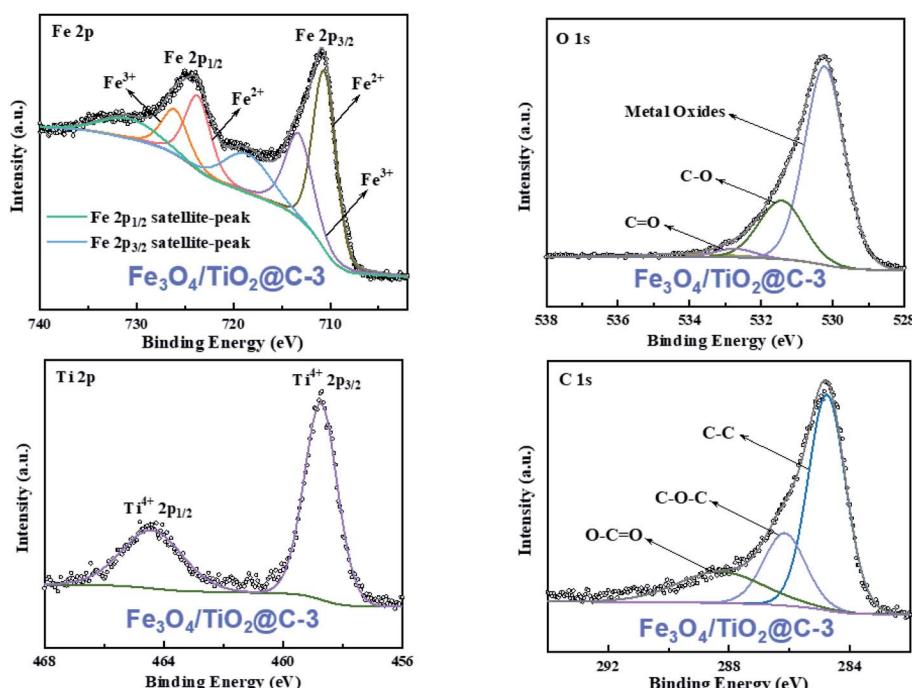

Fig. 4 High resolution XPS spectra of Fe_2p, Ti_2p, O1s and C1s of $Fe_3O_4/TiO_2@C$-3.

$TiO_2@C$-1, $Fe_3O_4/TiO_2@C$-2, $Fe_3O_4/TiO_2@C$-3 and $Fe_3O_4/TiO_2@C$-4 respectively, whereas the mass fraction of TiO_2 was 91.5%, 82.8%, 76.4% and 63.7%. As the titanium butoxide increases from 0.5 mL to 5 mL, the mass fraction of TiO_2 increases correspondingly.

EDX element mapping of $Fe_3O_4/TiO_2@C$-3 electrode was employed to investigate element distribution in $Fe_3O_4/TiO_2@C$ composites and is shown in Fig. S2 attached in the ESI.† Chemical composition of fabricated material is confirmed by uniform distribution of Ti, Fe, C and O in the scanned area, which indicates that Fe_3O_4 is evenly distributed on the surface of TiO_2 nanoarray, and carbon cloth is fully covered by Fe_3O_4/TiO_2 nanosized composites.

The element composition and valence information in the samples were detected by X-ray photoelectron spectroscopy (XPS). The XPS spectrum of $Fe_3O_4/TiO_2@C$-3 confirmed the presence of Fe, O, Ti and C in the sample (Fig. 3(a)). Fig. 4(a) shows the high-resolution spectra of Fe2p in $Fe_3O_4/TiO_2@C$ composites. The characteristic peaks of Fe2p at 710.8 and 724.4 eV correspond to the spin–orbit peaks of $Fe2p_{3/2}$ and $Fe2p_{1/2}$, which is in good agreement with previous reports.[36,37] Two satellite signals of $Fe2p_{3/2}$ and $Fe2p_{1/2}$ peaks were observed at the same time, which can be attributed to the oxidation states of Fe^{3+} and Fe^{2+} in Fe_3O_4 nanoparticles.[38,39] Two strong peaks of rutile type crystals are shown in the Ti2p spectra (Fig. 4(b)), and the binding energies are 458.8 eV (Ti^{3+}) and 464.5 eV (Ti^{4+}) respectively, which correspond to the two chemical energy levels of $Ti2p_{3/2}$ and $Ti2p_{1/2}$. The O1s peak in Fig. 4(c) at 530.7 eV is in accordance with the Ti–O–Ti bond, confirming the formation of rutile phase of TiO_2.[40] The C1s spectrum in Fig. 4(d) at high resolution can be deconvoluted into three peaks at 284.7, 286.2 and 288.6 eV, indicating the existence of C–C, C=O and O–C=O. The O1s spectrum can be deconvoluted into a larger oxide main at 530.1 eV and weaker peaks caused by C–O and C–O–C at

531.4 eV and 533.1 eV. The weaker carbon–oxygen interaction implies that the oxygen-containing functional groups of $Fe_3O_4/TiO_2@C$ has been removed during the calcination process. XPS results revealed the co-existence of rutile phase TiO_2 and magnetite Fe_3O_4 in $Fe_3O_4/TiO_2@C$ composite.

3.2 Electrochemical measurement

Fig. 5(a) displays the CV curves of $Fe_3O_4/TiO_2@C$-1 at scanning rates of 2.5, 5, 10, 25, and 50 mV s^{-1} in 1 M Na_2SO_3 solution with a potential window from −1.1 V to 0.15 V. The CV curve exhibits a distorted quasi-rectangular shape at different scan rates. As the scan rate increases from 2.5 mV s^{-1} to 50 mV s^{-1}, a similar rectangular shape is observed without obvious redox peaks, indicating a rapid charge/discharge process an ideal pseudo-capacitive behavior.[41–43] As the scan rate increases, the shape of the curve remains unchanged with an increase in the current density, which is in good agreement with the non-Faraday behavior. The slight deviation of the CV curve from the ideal rectangle is caused by the polarization of the hydrated alkaline particles at a larger scanning rate, which results in insufficient time for some alkaline particles to adsorb to the surface of $Fe_3O_4/TiO_2@C$.[44]

Galvano-static charge and discharge (GCD) experiments were also performed to further understand the supercapacitance properties of $Fe_3O_4/TiO_2@C$ electrode. The current densities of GCD during charge and discharge are 1 mA cm^{-2}, 2 mA cm^{-2}, 2.5 mA cm^{-2}, 5 mA cm^{-2} and 10 mA cm^{-2} and the result is shown in Fig. 5(b). It can be seen that the GCD curve at all current densities exhibits a good triangular symmetry, which proves that the capacity of the material is mainly derived from the capacitive behavior and is in good agreement with the result of the CV.[45,46] Besides, The GCD curve can be approximated as linear slope with tiny voltage drop, indicating that $Fe_3O_4/$
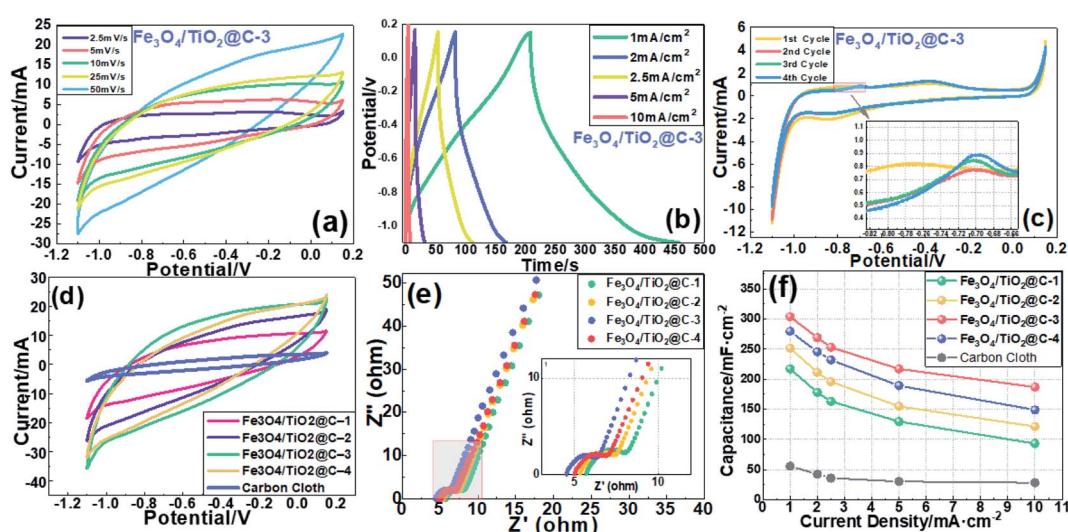

Fig. 5 (a) CV curves of $Fe_3O_4/TiO_2@C$-3 electrode at various scan rates, (b) GCD curves of $Fe_3O_4/TiO_2@C$-3 electrode at various current densities, (c) CV curves of $Fe_3O_4/TiO_2@C$-3 electrode at the beginning, (d) CV curves of $Fe_3O_4/TiO_2@C$-1, $Fe_3O_4/TiO_2@C$-2, $Fe_3O_4/TiO_2@C$-3, $Fe_3O_4/TiO_2@C$-4 and carbon cloth, (e) Nyquist plots of $Fe_3O_4/TiO_2@C$-1, $Fe_3O_4/TiO_2@C$-2, $Fe_3O_4/TiO_2@C$-3 and $Fe_3O_4/TiO_2@C$-4, (f) areal capacitances of $Fe_3O_4/TiO_2@C$-1, $Fe_3O_4/TiO_2@C$-2, $Fe_3O_4/TiO_2@C$-3, $Fe_3O_4/TiO_2@C$-4 and carbon cloth.

TiO$_2$@C electrode has excellent redox reversibility and good electrochemical stability.[47]

Fig. 5(c) describes the variation of CV curve in the initial four cycles of Fe$_3$O$_4$/TiO$_2$@C electrode at a scan rate of 2.5 mV s^{-1}. The contour shape of CV curve is basically the same, and the CV curve of the first cycle has the largest enclosed area. The most obvious difference is that the oxidation peak appears around -0.78 V in the first cycle and immediately disappears at the end of the cycle, while the oxidation peak in the subsequent cycles emerges around -0.7 V and its position remains unchanged. The first cycle oxidation peak is caused by the activation of the electrode surface and the accompanying irreversible redox reaction, which can be illustrated by the following equation:[48,49]

$$TiO_2 + Na^+ + e^- \rightarrow TiOONa \tag{3}$$

$$FeO_x(OH)_y + \delta Na^+ + \delta e^- \rightarrow Na_\delta FeO_x(OH)_y \tag{4}$$
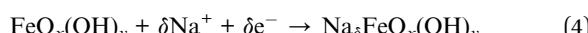
In the Fe$_3$O$_4$/TiO$_2$@C structure, Fe$_3$O$_4$ nanoparticles with high pseudocapacitance significantly promote the faradaic reaction on the electrode surface assisted by the TiO$_2$ nanorod arrays used as high-conductivity scaffold for Fe$_3$O$_4$ nanoparticles. Fully exposed TiO$_2$ increases the electroactive surface area and shorten the ion diffusion path length, which helps to achieve the remarkably capacitive performance of the composite electrode material.

Fig. 5(d) shows the CV curve of Fe$_3$O$_4$/TiO$_2$@C-1, Fe$_3$O$_4$/TiO$_2$@C-2, Fe$_3$O$_4$/TiO$_2$@C-3 and Fe$_3$O$_4$/TiO$_2$@C-4 at a scan rate of 50 mV s^{-1}. As can be seen from the figure, the surrounding area for each electrode follows the order of Fe$_3$O$_4$/TiO$_2$@C-4 < Fe$_3$O$_4$/TiO$_2$@C-2 < Fe$_3$O$_4$/TiO$_2$@C-3 < Fe$_3$O$_4$/TiO$_2$@C-1 whereas the Fe$_3$O$_4$/TiO$_2$@C-3 sample with an addition of 2.5 mL titanium butoxide displays the largest integrated area, indicating the synergistic effect between EDLC and faradaic capacitance of Fe$_3$O$_4$/TiO$_2$@C reaches maximum under this circumstance. The capacitance decreases as the titanium butoxide continues to increase, which may be caused by excess addition that leads to the formation of more crystal defects.[50,51] Fe$_3$O$_4$/TiO$_2$@C-4 with lowest TiO$_2$ precursor exhibits smallest integrated area of the CV curve among 4 Fe$_3$O$_4$/TiO$_2$@C electrodes, indicating the capacitance is largely relied on Fe$_3$O$_4$ and the corresponding Faraday reaction is the redox reaction of sulfur-containing anions on the surface of Fe$_3$O$_4$.[52] As the content of TiO$_2$ increases, the TiO$_2$ framework can provide more adsorption

sites for Fe$_3$O$_4$ and promote the insertion and extraction of Na$^+$ as well as the movement of Na$^+$ in staggered channels of TiO$_2$.

Electrochemical impedance spectroscopy (EIS) was carried out to study the electrochemical behavior of Fe$_3$O$_4$/TiO$_2$@C electrode. The Nyquist plot in Fig. 5(e) is composed of a semicircle in the high frequency range and a leaning line in the low frequency range. The intercept of the Nyquist curve and the horizontal axis is the solution resistance (R_s), of which the figures are 5.7 Ω, 5.3 Ω, 4.5 Ω and 5.0 Ω respectively for Fe$_3$O$_4$/TiO$_2$@C-1, 2, 3 and 4. The semicircle determines the charge transfer resistance (R_{ct}) at the interface between the electrode material and the electrolyte whereas the straight line in the low frequency region represents the ion diffusion resistance (*i.e.* Warburg resistance).[53,54] A low series resistance (R_s) was obtained by Fe$_3$O$_4$/TiO$_2$@C due to the *in situ* growth of TiO$_2$ on the porous carbon cloth substrate. The Fe$_3$O$_4$/TiO$_2$@C-1 electrode has the largest semicircle in the high-frequency range, suggesting a higher charge-transfer resistance of the electrode. Among all electrodes the Fe$_3$O$_4$/TiO$_2$@C-3 has the smallest R_{ct} and 1.36 Ω, 1.21 Ω, 1.05 Ω and 1.15 Ω were calculated respectively for Fe$_3$O$_4$/TiO$_2$@C-1, Fe$_3$O$_4$/TiO$_2$@C-2, Fe$_3$O$_4$/TiO$_2$@C-3 and Fe$_3$O$_4$/TiO$_2$@C-4. At the same time, the Fe$_3$O$_4$/TiO$_2$@C-3 electrode shows the largest slope, which means that the ion diffusion process is the fastest compared with its counterparts. The favoring feature can be attributed to the mesoporous Fe$_3$O$_4$/TiO$_2$@C nanostructure which increases the specific surface area and paves an easy and fast road for the ion transition on electrode/electrolyte interface. The direct contact between the Fe$_3$O$_4$ loaded TiO$_2$ nanorod arrays and the carbon cloth substrate also facilitates charge transfer and ensures full electrochemical utilization of electrode material.[54]

As shown in Fig. 5(f), it can be seen that the Fe$_3$O$_4$/TiO$_2$@C-3 composite material has the highest areal capacitance value at various current densities and a desirable areal capacitance of 304.1 mF cm^{-2} at current density of 1.0 mA cm^{-2}, which results from the large specific surface area of the unique structure and low inner resistance. On the other hand, even at the highest current density (10 mA cm^{-2}), Fe$_3$O$_4$/TiO$_2$@C-3 still displays a high capacitance of 186.9 mF cm^{-2}, which is attributed to the fact that TiO$_2$ nanorod array provides an efficient and fast electron transport channel and gives full play to the pseudocapacitive effect of Fe$_3$O$_4$. The areal capacitance of other Fe$_3$O$_4$/TiO$_2$@C calculated according to the GCD results are 217.2 mF cm^{-2} (Fe$_3$O$_4$/TiO$_2$@C-1), 251.6 mF cm^{-2} (Fe$_3$O$_4$/TiO$_2$@C-2) and
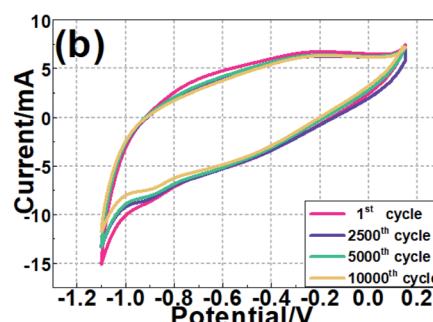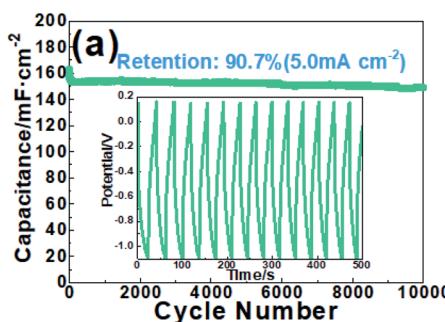

Fig. 6   (a) Cycling stability of the Fe$_3$O$_4$/TiO$_2$@C-3 electrode, (b) comparable CV measurement at various cycle stages.
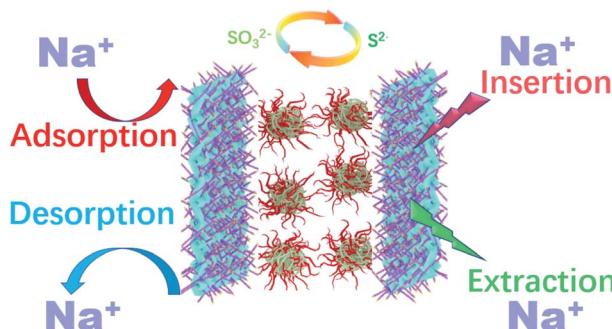
Fig. 7 Energy storage mechanism in symmetrical $Fe_3O_4/TiO_2@C$ supercapacitors.

279.8 mF cm^{-2} ($Fe_3O_4/TiO_2@C$-4) respectively at current density of 1.0 mA cm^{-2}. At each charge/discharge current density, specific capacitance of the electrode decreases in the order of $Fe_3O_4/TiO_2@C$-3, $Fe_3O_4/TiO_2@C$-4 $Fe_3O_4/TiO_2@C$-2 and $Fe_3O_4/TiO_2@C$-1. These results are consistent with the order of the area enclosed by the CV curve in Fig. 5(d).

The long-term cycling stability of $Fe_3O_4/TiO_2@C$-3 electrode at a charge/discharge current density of 5.0 mA cm^{-2} is shown in Fig. 6(a). The result indicates the areal capacity of $Fe_3O_4/TiO_2@C$ electrode decreases gradually from 163.97 mF cm^{-2} to 148.72 mF cm^{-2} with a capacity retention rate of 90.7% after 10 000 cycles. For comparison, cycle number of 1, 2500, 5000 and 10 000 were selected to perform *ex situ* CV measurement respectively and the result is shown in Fig. 6(b). It can be seen that the CV curves are approximately coincident with only slight differences in the enclosed areas. The cycling performance of $Fe_3O_4/TiO_2@C$ electrode is probably attributed to the combined effect of TiO_2–C nanowire array and Fe_3O_4 nanoparticles in the self-assembled electrode. The slight decrease may be attributed to the repeated expansion and contraction of the electrode material and the accumulation of structural defects during charge and discharge. The good cycle stability of the device indicates that it has practical potential in supercapacitor applications. To compare experimental data with theoretical capacity, the result of the integral area and areal capacitance of each period calculated according to eqn (2) is listed in Table S3 in ESI.†

As is shown in the Table S3,† the areal capacitance calculated according to the integrated area are 155.24 mF cm^{-2}, 149.67 mF cm^{-2}, 145.22 mF cm^{-2} and 138.81 mF cm^{-2} at cycle number of 1, 2500, 5000 and 10 000 respectively. Calculated capacitance according to integrated area is in good agreement with the

tested data, and the retention rate 89.4% is approximately the same as experiment result (90.7%). Combined with the long-time stability test and *ex situ* CV measurement, it is convincing that $Fe_3O_4/TiO_2@C$ has unique advantages in terms of high capacitance and good cycling stability. Specific capacitance data calculated by load mass is also provided in Table S4† for comparison with areal capacitance.

The excellent electrochemical performance of $Fe_3O_4/TiO_2@C$ is revealed by the following aspects. The charge storage capacity of Fe_3O_4 nanoparticles was improved when combined with vertical TiO_2 nanorods. Typical EDLC behavior was observed from the rectangular shape of the CV curve and the linear dependence of voltage on time in the GCD curve, which demonstrates pure capacitive behavior and pseudo-capacitance effect are simultaneously achieved on $Fe_3O_4/TiO_2@C$ electrode. Fe_3O_4 anchored TiO_2 introduces and redox contribution in the charge storage mechanism, which is confirmed in CV curve and GCD measurement. In $Fe_3O_4/TiO_2@C$, the contribution of charge storage can be attributed to two synergistic mechanisms. The first is the Faraday reaction caused by the insertion and deintercalation of Na^+ and sulfur-containing anions in the electrolyte, which occurs during the charging and discharging process of supercapacitors, while the second principle is the adsorption of Na^+ ions on $Fe_3O_4/TiO_2@C$ surface.

Working principle of $Fe_3O_4/TiO_2@C$ in Na_2SO_3 electrolyte is illustrated in Fig. 7. The improvement of $Fe_3O_4/TiO_2@C$ sample performance can be related to the optimized hybrid nanorod array obtained *via* hydrothermal process, where the addition of titanium butoxide promotes the formation of TiO_2 nanorod arrays. As more TiO_2 are introduced, the array configuration begins to gather, and adjacent nanorods are interwoven to form a micro-flower structure. The micro-flower structure is assembled on the surface of carbon cloth assisted by the non-vertical growth of TiO_2 nanorods, and the unique architecture further increases the electrochemically active area. Moreover, the micro-flower structure provides a fast electron transmission path, thereby increasing the conductivity and reducing charge transfer resistance. In addition, the nanostructured Fe_3O_4/TiO_2 possesses more electrolyte diffusion channels, which is beneficial for the electrolyte ions to fully enter the inside of the active material. The optimized morphology makes the entry of electrolyte ions more effective and provides more sites for ion adsorption. Particularly, the direct contact between TiO_2 and the carbon cloth takes full advantages of interfacial bonding between substrate and Fe_3O_4/TiO_2 nanocomposite and facilitating electron migration with minor obstacles.

Table 1 Comparison of the similar electrodes in supercapacitor application

Electrode	Electrolyte	Current density	Specific capacitance	Retention rate	Reference
N-Doped TiO_2	1.0 M KOH	4.0 mA cm^{-2}	177.1 mF cm^{-2}	83.6%	55
$MoS_2@TiO_2$	1.0 M Na_2SO_4	0.2 A g^{-1}	428.1 F g^{-1}	97.0%	56
$TiO_2@MnO_2$	0.5 M Na_2SO_4	0.5 A g^{-1}	150.9 mF cm^{-2}	71.4%	57
$Co(OH)_2/TiO_2$	2.0 M KOH	1.0 mA cm^{-2}	148.0 mF cm^{-2}	82.5%	58
$Fe_3O_4/TiO_2@C$	1 M Na_2SO_3	1.0 mA cm^{-2}	304.1 mF cm^{-2}	93.1%	This work

The capacitance of several TiO_2-based nanocomposite supercapacitor used in aqueous environment has been summarized. Table 1 lists the attained specific capacitance, retention rate and their comparison with previous reports. Compared with the other materials from literature, synthesized $Fe_3O_4/TiO_2@C$ within this work exhibits relatively high areal capacitance and desirable retention rate, which proves it to be a competitive candidate for energy storage applications.

4. Conclusions

In summary, Fe_3O_4/TiO_2 nanorod arrays grown on carbon cloth ($Fe_3O_4/TiO_2@C$) substrate has been successfully prepared *via* a reasonable hydrothermal-chemical deposition method. Notably, the prepared nanostructured composites are directly used without binder as flexible electrode for asymmetric sodium-ion supercapacitors. Meanwhile, samples with different Fe_3O_4/TiO_2 mass ratios were also prepared to explore the optimum synthesis concentration by adding different TiO_2 precursor solutions. Benefiting from the efficient pseudocapacitive properties of Fe_3O_4/TiO_2 and the interconnected effect between TiO_2 arrays and conductive carbon network, the assembled asymmetric supercapacitor exhibits areal capacitance of 304.1 mF cm^{-2} at a current density of 1.0 mA cm^{-2} in the operating voltage window from -1.1 V to 0.15 V and excellent cycling stability with only 9.3% capacitance deterioration after 10 000 cycles at high current density of 5.0 mA cm^{-2}. The impressive electrochemical performance can be attributed to the well-aligned array structure, increased redox-active surface area and uniformly connected arrangement of the binary metal oxides. Hence, porous carbon cloth is functionalized as the conductive framework which provides flexibility for binder-free electrode. Therefore, the presentation of $Fe_3O_4/TiO_2@C$ with enhanced capacitance and stable cycle life provides a novel strategy for developing flexible electronic devices in energy storage and conversion applications.

Conflicts of interest

There are no conflicts to declare.

References

1 S. Karthikeyan, B. Narenthiran, A. Sivanantham, L. D. Bhatlu and T. Maridurai, *Mater. Today: Proc.*, 2021, DOI: 10.1016/j.matpr.2021.02.526.

2 J. Xu, F. Zheng, C. Xi, Y. Yu, L. Chen, W. Yang, P. Hu, Q. Zhen and S. Bashir, *J. Power Sources*, 2018, **404**, 47–55.

3 M. Bigdeloo, E. Kowsari, A. Ehsani, A. Chinnappan, S. Ramakrishna and R. AliAkbari, *J. Energy Storage*, 2021, **37**, 102474.

4 R. R. Salunkhe, Y. V. Kaneti and Y. Yamauchi, *ACS Nano*, 2017, **11**, 5293–5308.

5 A. Mohanty, D. Jaihindh, Y.-P. Fu, S. P. Senanayak, L. S. Mende and A. Ramadoss, *J. Power Sources*, 2021, **488**, 229444.

6 B. K. Saikia, S. M. Benoy, M. Bora, J. Tamuly, M. Pandey and D. Bhattacharya, *Fuel*, 2020, **282**, 118796.

7 W. Zhang, R.-r. Cheng, H.-h. Bi, Y.-h. Lu, L.-b. Ma and X.-j. He, *New Carbon Mater.*, 2021, **36**, 69–81.

8 V. Petrić and Z. Mandić, *Electrochim. Acta*, 2021, **384**, 138372.

9 K. Nasrin, S. Gokulnath, M. Karnan, K. Subramani and M. Sathish, *Energy Fuels*, 2021, **35**, 6465–6482.

10 R. Hajare, S. Kempahanumakkagaari, T. Ramakrishnappa, A. Saniya, K. Sourav and A. Amrutha, *Mater. Today: Proc.*, 2021, DOI: 10.1016/j.matpr.2021.05.164.

11 D. Wei, M. R. Scherer, C. Bower, P. Andrew, T. Ryhänen and U. Steiner, *Nano Lett.*, 2012, **12**, 1857–1862.

12 L. Miao, Z. Song, D. Zhu, L. Li, L. Gan and M. Liu, *Energy Fuels*, 2021, **35**, 8443–8455.

13 S. A. Delbari, L. S. Ghadimi, R. Hadi, S. Farhoudian, M. Nedaei, A. Babapoor, A. S. Namini, Q. Van Le, M. Shokouhimehr and M. S. Asl, *J. Alloys Compd.*, 2020, 158281.

14 K. S. Kumar, N. Choudhary, Y. Jung and J. Thomas, *ACS Energy Lett.*, 2018, **3**, 482–495.

15 R. Wang, X. Li, Z. Nie, Y. Zhao and H. Wang, *J. Energy Storage*, 2021, **38**, 102479.

16 M. K. Paliwal and S. K. Meher, *ACS Appl. Nano Mater.*, 2020, **3**, 4241–4252.

17 J. Ming, H. Ming, W. Yang, W.-J. Kwak, J.-B. Park, J. Zheng and Y.-K. Sun, *RSC Adv.*, 2015, **5**, 8793–8800.

18 S. Su, L. Lai, R. Li, Y. Lin, H. Dai and X. Zhu, *ACS Appl. Energy Mater.*, 2020, **3**, 9379–9389.

19 L. Zheng, Y. Dong, H. Bian, C. Lee, J. Lu and Y. Y. Li, *Electrochim. Acta*, 2016, **203**, 257–264.

20 X. Lu, M. Yu, G. Wang, T. Zhai, S. Xie, Y. Ling, Y. Tong and Y. Li, *Adv. Mater.*, 2013, **25**, 267–272.

21 Z. Yi, Q. Han, P. Zan, Y. Cheng, Y. Wu and L. Wang, *J. Mater. Chem. A*, 2016, **4**, 12850–12857.

22 A. Ramadoss, G.-S. Kim and S. J. Kim, *CrystEngComm*, 2013, **15**, 10222–10229.

23 S. Sundriyal, M. Sharma, A. Kaur, S. Mishra and A. Deep, *J. Mater. Sci.: Mater. Electron.*, 2018, **29**, 12754–12764.

24 L.-l. Jiang, X. Lu, C.-m. Xie, G.-j. Wan, H.-p. Zhang and T. Youhong, *J. Phys. Chem. C*, 2015, **119**, 3903–3910.

25 C. C. Raj, V. Srimurugan, A. Flamina and R. Prasanth, *Mater. Chem. Phys.*, 2020, **248**, 122925.

26 Y.-J. Gu, W. Wen and J.-M. Wu, *J. Power Sources*, 2020, **469**, 228425.

27 Q. Wang, J. Wang, H. Wang, J. Zhan, Y. Zhu, Q. Zhang, Q. Shen and H. Yang, *Appl. Surf. Sci.*, 2019, **493**, 1125–1133.

28 Y. Cao, W. Yang, M. Wang, N. Wu, L. Zhang, Q. Guan and H. Guo, *Int. J. Hydrogen Energy*, 2021, **46**, 18179–18206.

29 R. Zhang, C. Chen, H. Yu, S. Cai, Y. Xu, Y. Yang and H. Chang, *J. Electroanal. Chem.*, 2021, **893**, 115323.

30 Z. Li, B. Wang, Y. Tian, X. Zhao, Q. Guo and G. Nie, *Synth. Met.*, 2021, **277**, 116785.

31 R. Liu, W. Guo, B. Sun, J. Pang, M. Pei and G. Zhou, *Electrochim. Acta*, 2015, **156**, 274–282.

32 X. Hu, M. Ma, M. Zeng, Y. Sun, L. Chen, Y. Xue, T. Zhang, X. Ai, R. G. Mendes and M. H. Rümmeli, *ACS Appl. Mater. Interfaces*, 2014, **6**, 22527–22533.

33 S. Li, H. Jiang, K. Yang, Z. Zhang, S. Li, N. Luo, Q. Liu and R. Wei, *J. Alloys Compd.*, 2018, **746**, 670–676.

34 R. Hatefi, H. Younesi, A. Mashinchian-Moradi and S. Nojavan, *Adv. Powder Technol.*, 2021, **32**, 2410–2422.

35 H. Fan, G. Yi, X. Zhang, B. Xing, C. Zhang, L. Chen and Y. Zhang, *Opt. Mater.*, 2021, **111**, 110582.

36 L. Wang, F. Liu, A. Pal, Y. Ning, Z. Wang, B. Zhao, R. Bradley and W. Wu, *Carbon*, 2021, **179**, 327–336.

37 S. Venkateswarlu, H. Mahajan, A. Panda, J. Lee, S. Govindaraju, K. Yun and M. Yoon, *Chem. Eng. J.*, 2020, 127584.

38 J. Patra, S.-C. Wu, I.-C. Leu, C.-C. Yang, R. S. Dhaka, S. Okada, H.-L. Yeh, C.-M. Hsieh, B. K. Chang and J.-K. Chang, *ACS Appl. Energy Mater.*, 2021, **4**, 5738–5746.

39 H. Mao, J. Sun, E. Bao, L. Dai, C. Xu and H. Chen, *Ceram. Int.*, 2021, DOI: 10.1016/j.ceramint.2021.05.214.

40 S. A. Pawar, D. S. Patil and J. C. Shin, *Curr. Appl. Phys.*, 2019, **19**, 794–803.

41 Q. Xu, C. Lu, S. Sun and K. Zhang, *J. Phys. Chem. Solids*, 2019, **129**, 234–241.

42 Y. Qu, X. Tong, C. Yan, Y. Li, Z. Wang, S. Xu, D. Xiong, L. Wang and P. K. Chu, *Vacuum*, 2020, **181**, 109648.

43 S. Ramanathan, M. SasiKumar, N. Radhika, A. Obadiah, A. Durairaj, G. H. Swetha, P. Santhoshkumar, I. S. Lydia and S. Vasanthkumar, *Mater. Today: Proc.*, 2021, DOI: 10.1016/j.matpr.2021.01.706.

44 E. Payami and R. Teimuri-Mofrad, *Electrochim. Acta*, 2021, **383**, 138296.

45 S. Sundriyal, V. Shrivastav, M. Sharma, S. Mishra and A. Deep, *J. Alloys Compd.*, 2019, **790**, 377–387.

46 W. Zhong, H. Sun, J. Pan, Y. Zhang, X. Yan, Y. Guan, W. Shen and X. Cheng, *Mater. Sci. Semicond. Process.*, 2021, **127**, 105715.

47 A. Kumar, D. Sarkar, S. Mukherjee, S. Patil, D. Sarma and A. Shukla, *ACS Appl. Mater. Interfaces*, 2018, **10**, 42484–42493.

48 H. Wang, X. Xu, C. Wang, A. Neville and Y. Hua, *Energy Fuels*, 2021, **35**, 8406–8416.

49 P. Sun, X. Zhang, C. Wang, Y. Wei, L. Wang and Y. Liu, *J. Mater. Chem. A*, 2013, **1**, 3309–3314.

50 J. Liu, Y. Wang, M. Wang, C. Pei, M. Cui, Y. Yuan, G. Han, B. Liu, H. Zhao and H. Yang, *J. Alloys Compd.*, 2018, **749**, 543–555.

51 Y. Gawli, A. Banerjee, D. Dhakras, M. Deo, D. Bulani, P. Wadgaonkar, M. Shelke and S. Ogale, *Sci. Rep.*, 2016, **6**, 1–10.

52 H. A. Ghaly, A. G. El-Deen, E. R. Souaya and N. K. Allam, *Electrochim. Acta*, 2019, **310**, 58–69.

53 S. Ramanathan, S. Moorthy, S. Ramasundaram, H. K. Rajan, S. Vishwanath, S. Selvinsimpson, A. Durairaj, B. Kim and S. Vasanthkumar, *ACS Omega*, 2021, **6**, 14734–14747.

54 I. Khan and A. Qurashi, *ACS Sustainable Chem. Eng.*, 2018, **6**, 11235–11245.

55 X. Su, Q. He, Y.-e. Yang, G. Cheng, D. Dang and L. Yu, *Diamond Relat. Mater.*, 2021, **114**, 108168.

56 J. Zhou, M. Guo, L. Wang, Y. Ding, Z. Zhang, Y. Tang, C. Liu and S. Luo, *Chem. Eng. J.*, 2019, **366**, 163–171.

57 H. Zhou, X. Zou and Y. Zhang, *Electrochim. Acta*, 2016, **192**, 259–267.

58 A. Ramadoss and S. J. Kim, *Electrochim. Acta*, 2014, **136**, 105–111.